Key Points:
- TGF duration and number of avalanches define the shape and internal noise level in the energy spectrum of the TGF source current moment
- Modulation of VLF spectrum by multiplicity of TGF peaks is consistent with observed VLF sferics simultaneous with such multipeak TGFs
- VLF measurements can give the estimate for the number of avalanches in longer lasting TGFs

Spectral Characteristics of VLF Sferics Associated With RHESSI TGFs

Andrew Mezentsev[1] [ID], **Nikolai Lehtinen[1]** [ID], **Nikolai Østgaard[1]** [ID], **F. J. Pérez-Invernón[2]** [ID], and **Steven A. Cummer[3]** [ID]

[1]Birkeland Centre for Space Science, Department of Physics and Technology, University of Bergen, Bergen, Norway, [2]Instituto de Astrofísica de Andalucía, CSIC, Granada, Spain, [3]Electrical and Computer Engineering Department, Duke University, Durham, NC, USA

Abstract We compared the modeled energy spectral density of very low frequency (VLF) radio emissions from terrestrial gamma ray flashes (TGFs) with the energy spectral density of VLF radio sferics recorded by Duke VLF receiver simultaneously with those TGFs. In total, six events with world wide lightning location network (WWLLN) defined locations were analyzed to exhibit a good fit between the modeled and observed energy spectral densities. In VLF range the energy spectral density of the TGF source current moment is found to be dominated by the contribution of secondary low-energy electrons and independent of the relativistic electrons which play their role in low-frequency (LF) range. Additional spectral modulation by the multiplicity of TGF peaks was found and demonstrated a good fit for two TGFs whose VLF sferics consist of two overlapping pulses each. The number of seeding pulses in TGF defines the spectral shape in VLF range, which allows to retrieve this number from VLF sferics, assuming they were radiated by TGFs. For two events it was found that the number of seeding pulses is small, of the order of 10. For the rest of the events the lower boundary of the number of seeding pulses was found to be between 10 to 10^3.

1. Motivation

Terrestrial gamma ray flashes (TGFs) are the bursts of energetic photons coming out from the Earth's atmosphere to space (Fishman et al., 1994). The possibility of the accompanying radio frequency (RF) emission generated by the TGF producing relativistic electrons and their byproduct currents is currently actively discussed. The latest observations, modeling, and theoretical analysis tend to associate the TGF production with the early stage of the positive in-cloud (+IC) discharge, when the negative stepped leader is propagating upward (Celestin et al., 2012, 2015; Celestin & Pasko, 2011; Connaughton et al., 2013; Cummer et al., 2014, 2015, 2005; Dwyer & Cummer, 2013; Lu et al., 2010, 2011; Lyu et al., 2016; Mezentsev et al., 2016; Shao et al., 2010; Stanley et al., 2006; Xu et al., 2014, 2012).

The main target of this work is to establish theoretically and test on real measurements a link between TGF properties (as observed from space) and ground-measured characteristics of very low frequency (VLF) sferics related to TGFs. This is important in the context of the latest efforts on distant remote sensing of TGFs by the use of (presumably) their radio emissions (Lyu et al., 2016). Also, a TGF structure might have hidden levels of organization which are hard or impossible to resolve from satellite observations, but which may manifest themselves in the radio emissions produced by the TGF sources.

TGF detection and recognition by their radio signatures need a correct theory of TGF radio emission, verified by relevant statistics of simultaneous observations of both: TGFs and their radio signatures. In this work we use the TGF radio emission model developed in Dwyer and Cummer (2013). Our main goal is to reveal evident connection between the real TGFs and their radio emissions. So far, this problem has not been presented in the literature as a comprehensive view, instead analyzing TGF-VLF simultaneity itself (Connaughton et al., 2010; Cummer et al., 2011), studying TGF-VLF simultaneity with emphasis on TGF properties (Connaughton et al., 2013), or performing some statistical analysis of the radio sferic properties without sufficient linking to TGF properties (Lyu et al., 2016).

In this work, based on the model developed in Dwyer and Cummer (2013), we analyze the energy spectral density (which for brevity hereafter we call just "energy spectrum") of the TGF source current moment,

figure out the relative importance of different types of currents constituting a TGF and their contributions into the spectrum in different frequency ranges. We found that the VLF range contains the most essential information about TGF structure and gives the link between the TGF temporal parameters (like duration, peak multiplicity, and separation times between peaks) and the energy spectrum of the VLF sferic emitted by the TGF.

We apply the results of our analysis to six TGFs detected by Reuven Ramaty High Energy Solar Spectroscopic Imager (RHESSI) with simultaneously recorded VLF sferics with source locations determined by World Wide Lightning Location Network (WWLLN). Distance range between the source and the VLF receiver of 2,000 to 4,000 km makes the consideration of the propagation effects in the Earth-ionosphere waveguide (EIWG) an essential part of our work.

The results of the presented analysis allow us to address the question of the TGF structure. Indeed, for understanding the nature of a TGF source it is important to know if a TGF is formed by a continuous (yet somehow modulated) flux of relativistic electrons, or it consists of a sequence (somehow modulated) of distinct pulses. As long as the observed TGF spectra require the multiplication of runaway electrons in the strong E field by the relativistic runaway electron avalanche (RREA) process, the question of the TGF structure becomes the question of a structure of the flux of seeding relativistic electrons injected in the high E field region. The TGF radio emission model (Dwyer & Cummer, 2013) indicates that these two cases (a continuous flux and a sequence of pulses) have to produce essentially different energy spectra of the source current moments. Also, in case of a pulsed nature of the seeding flux the RF emission energy spectra make it possible to estimate the number of those seeding pulses, at least within an order of magnitude. With certain limitations this value can be assessed from the real VLF sferics emitted by TGFs, which is supported by our results. This is important, because it relates directly to the number of pulses that constitute a TGF, which, in turn, refers to possible physical processes that underlie TGF generation.

In section 2 we introduce (without derivations) the spectrum of a TGF source current moment, proposed in the model of Dwyer and Cummer (2013). We discuss the structure of this spectrum with special focus on its VLF part and underlying source currents. There we also introduce the spectral modulation by the multiplicity of TGF peaks and describe the method of calculating the EIWG transfer function. Section 3 briefly describes the data used in the analysis. Results are summarized in section 5. Possible interpretations, implications, difficulties, and open questions are highlighted in section 6.

2. Theory

To model the radio frequency (RF) emissions produced by the TGFs as they would be observed by the Duke VLF receiver, we apply the theoretical framework presented by Dwyer and Cummer (2013). The observed azimuthal magnetic field energy spectrum $|B_\varphi(\omega)|^2$ is a product of three terms:

$$|B_\varphi(\omega)|^2 = |K(\omega)|^2 \cdot |F_{EIWG}(\omega)|^2 \cdot |F_{VLF}(\omega)|^2, \tag{1}$$

where $K(\omega)$ is the spectrum of the TGF source current moment, propagation effects are described by the EIWG transfer function $F_{EIWG}(\omega)$, and $F_{VLF}(\omega)$ characterizes the Duke VLF receiver's frequency response. Note that frequency response function of the VLF instrument $F_{VLF}(\omega)$ is dimensionless, while the physical unit for the EIWG transfer function $F_{EIWG}(\omega)$ is by definition equal to the ratio between the units of the magnetic field spectrum and the current moment spectrum, $[F_{EIWG}(\omega)]=[T/(A\ m)]$.

2.1. Source Current Moment Spectrum

To model a TGF source current moment, Dwyer and Cummer (2013) consider a TGF to be a superposition of a certain amount of individual RREAs. Each RREA is seeded by its individual pulse of seeding runaway electrons. When a seeding pulse develops into a RREA in the multiplication zone of a high E field, the runaway electrons ionize the air molecules producing the low-energy electrons and different types of ions. These runaway and low-energy electrons and ions experience the acceleration by the ambient E field and constitute the current pulses that generate radio emission which is understood as a radio emission of a TGF.

Here we briefly describe (without derivations) the structure of the energy spectrum of the TGF source current moment as it follows from the model, and the physical meaning of its components. Detailed descriptions and derivations can be found in the original work of Dwyer and Cummer (2013, and references therein).

Dwyer and Cummer (2013) use linear consideration of the problem (meaning that all differential equations for all species' charge densities are linear). This approach allows to represent the total current moment of the TGF source as a result of two consecutive convolutions between the current moment of a RREA seeded by a single particle, the total flux of seeding electrons, and the full current composition term, which accounts for the contributions of relativistic electrons, low-energy electrons, and positive and negative ions. In the frequency domain such a representation transforms into a consecutive product of the spectra of these three terms, which makes possible the analytical consideration of the TGF source spectrum.

The energy spectrum of the TGF source current moment $|K(f)|^2$, as a function of natural frequency $f = \omega/2\pi$, can be written as

$$|K(f)|^2 = K_0^2 \cdot \exp\left(-\frac{f^2}{f_A^2}\right) \cdot \left[\frac{N_p - 1}{N_p}\exp\left(-\frac{f^2}{f_B^2}\right) + \frac{1}{N_p}\right] \cdot |C(f)|^2. \tag{2}$$

The energy spectrum of the TGF source current moment is given by a product of the *amplitude term* K_0^2; the *RREA term*, which introduces the first cutoff frequency f_A; the *seeding flux term*, which is defined by the second cutoff frequency f_B and by the number of seeding pulses N_p; and the *total current composition term* $|C(f)|^2$. The amplitude term K_0^2 has the dimension $|K(f)|^2$, which is $(\text{A m/Hz})^2$, or equivalent to $(\text{C m})^2$ (see equation (3)). All other terms are dimensionless.

The amplitude K_0 of the total current moment spectrum is proportional to the total path length Ω of all runaway electrons in a TGF:

$$K_0^2 = e^2\Omega^2, \tag{3}$$

where e is the electronic charge. The quantity Ω is defined as an integral of the total number of runaway electrons along the TGF propagation path:

$$\Omega = \int N_{re}(z)\mathrm{d}z, \tag{4}$$

where $N_{re}(z)$ is the number of runaway electrons as a function of position z. The assumed linear model of the electric field gives the Gaussian profile for $N_{re}(z)$, which results in

$$\Omega^2 = 2\pi\kappa^2 N_{\text{TGF}}^2, \tag{5}$$

where N_{TGF} is the total number of runaway electrons in a TGF, and κ is the vertical thickness of a RREA (see Dwyer & Cummer, 2013, for details).

The RREA term is based on the linear approximation of the electric field in the avalanche zone, which gives a Gaussian profile for the number of runaway electrons as a function of the position at the end of the avalanche region. This leads to a Gaussian-like term in the spectrum with the first cutoff frequency f_A. This cutoff frequency f_A is defined by the characteristic duration (κ/v) of a RREA and by the characteristic duration σ_s of a seeding pulse:

$$f_A = \frac{1}{2\pi}\left(\frac{\kappa^2}{v^2} + \sigma_s^2\right)^{-\frac{1}{2}}. \tag{6}$$

Here κ is the vertical thickness of a RREA and v is the RREA velocity which is assumed to be $v = 0.89c$, where c is the speed of light in vacuum.

The seeding flux term characterizes the time profile of the seeding flux (and, consequently, the time profile of the TGF) and is based on the assumption that the total flux of the seeding particles is organized into N_p Gaussian pulses with duration σ_s each. Time distribution of these pulses follows a certain time profile $f_{\text{TGF}}(t)$ which describes the (single-peak) TGF time structure at the source. Considering the energy spectrum of the total flux of the seeding pulses as an ensemble average over the population of similar TGFs defined by the source function $f_{\text{TGF}}(t)$, we get the energy spectrum of the source function with an additive constant noise (due to fluctuations of the individual seeding pulses distribution) on the level of $1/N_p$ which starts from frequency f_{N_p} (see section 2.5 for details and equation (13)). Thereby, the number of seeding pulses (or the number of avalanches) N_p defines the radio visibility of a TGF in the higher VLF band, namely, within the range between f_{N_p} and f_A frequencies. For example (see section 5), in case when the number of seeding pulses N_p exceeds a certain value (which for our range of source distances is not very high, $\geq 10^3$), the VLF noise level of such a
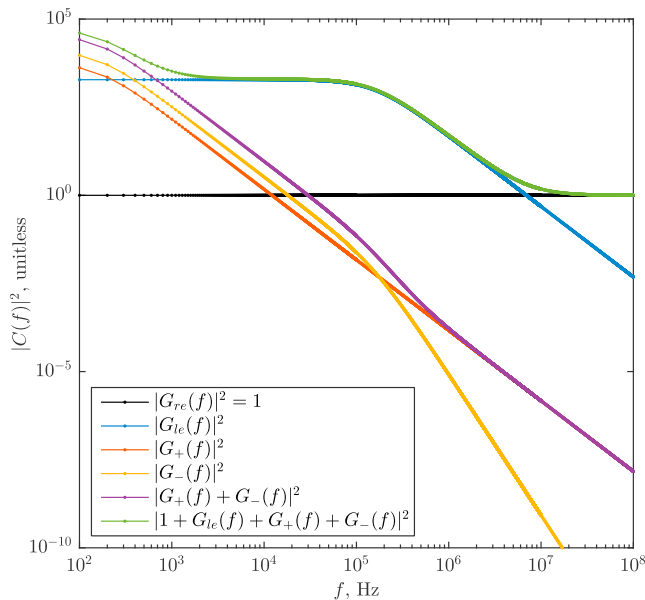
Figure 1. Energy spectrum of the total current composition term $|C(f)|^2$ shows relative contributions of different particles created by a single runaway electron into the energy spectrum of the source current moment. Black line shows the runaway electron. Blue line corresponds to the low-energy electrons. Red, yellow, and purple lines describe the contributions of the positive ions, negative ions, and their sum correspondingly. Green line represents the total current composition.

TGF becomes lower than the level of the natural VLF radio noise, and the radio signal from such a TGF should disappear in the considered frequency range.

Assuming a Gaussian profile for $f_{TGF}(t)$, we get a second cutoff frequency f_B, which is defined by the duration of a TGF σ_{TGF} at the source:

$$f_B = \frac{1}{2\pi\sigma_{TGF}}. \tag{7}$$

The total current composition term $C(\omega)$ *is defined by the dynamics of the secondary particles produced by a single runaway electron. Assuming linearity for both, the low-energy electrons and light ions, we get the spectrum of this term as*

$$C(\omega) = 1 - \frac{E\alpha(\mu_e - \mu_-)}{i\omega - \frac{1}{\tau}} - \frac{E\alpha(\mu_+ + \mu_-)}{i\omega - \frac{1}{\tau_{ion}}}. \tag{8}$$

This spectrum for simplicity was calculated for the constant electric field E and depends linearly on the ionization rate α (the number of electron-ion pairs created per unit length per runaway electron) and low-energy electrons and light ions mobilities μ_e, μ_+, and μ_-. This term also depends on two characteristic time constants τ and τ_{ion}, which characterize the low-energy electrons attachment time and the ion-ion recombination time correspondingly (see Dwyer & Cummer, 2013, for details).

Figure 1 shows the structure of the $|C(f)|^2$ term. Black horizontal line stands for the runaway electron contribution. Blue line describes the low-energy electrons created during propagation of the runaway electron. Their contribution dominates between 2 kHz and 1 MHz. The characteristic attachment time τ of the low-energy electrons to oxygen molecules is about 1 μs (Dwyer & Cummer, 2013) which leads to an exponential decay of the spectrum above 1 MHz. Red, yellow, and purple lines represent the contributions of the positive ions, negative ions, and their sum correspondingly. The ion contribution is dominant in the ULF and lower ELF frequency range (below 1 kHz), which is due to the adopted value of characteristic ion relaxation time τ_{ion} of 1 ms. Green line shows the total current composition term which combines all the contributions.

The structure of the energy spectrum (2) of the TGF source current moment $|K(f)|^2$ and the role of each term is illustrated in Figure 2. This figure consecutively introduces the total current composition (blue line); the influence of the individual RREA pulses with its higher end cutoff frequency f_A (red line); the influence of the TGF source time profile $f_{TGF}(t)$ with its lower end cutoff frequency f_B (purple line); and finally, the influence of random fluctuations in the individual avalanche pulses distribution with its flat shoulder starting at frequency f_{N_p} (green line). Characteristic frequencies of the spectrum are highlighted by the black vertical dashed lines. The gray background rectangle shows the frequency range of the observed VLF sferics (see details below). One should keep in mind that very large values of N_p lead to the flat shoulder (green curve in Figure 2) which is well below the natural EM noise level (not shown in the figure) and, thus, becomes nonobservable (see details below).

2.2. Modulation by Multiplicity of TGF

In case of a complex TGF time profile the source spectrum experiences additional modulation. Consider that a TGF has a complex structure and consists of N peaks (schematics of a TGF consisting of three separate peaks is shown in Figure 3). To simplify calculations, we assume that all *seeding pulses* in all TGF peaks are identical Gaussian pulses of width σ_s with the number of seeding particles N_{seed} in each seeding pulse. Each TGF peak may have its own number of seeding pulses N_{p_k} which follow the time profile of the corresponding TGF peak $f_k(t)$. Given these assumptions we can perform the ensemble averaging in the general case of a TGF consisting of N peaks with weights α_k, number of seeding pulses N_{p_k}, and the time profile $f_k(t)$ for the kth peak. The time separation between the kth and lth peaks is $\Delta t_{kl} = t_k - t_l$, where t_k is the peak time of the time profile $f_k(t)$ of the kth TGF peak. Also, we assume that the time profile of each TGF peak is an even function relative to its
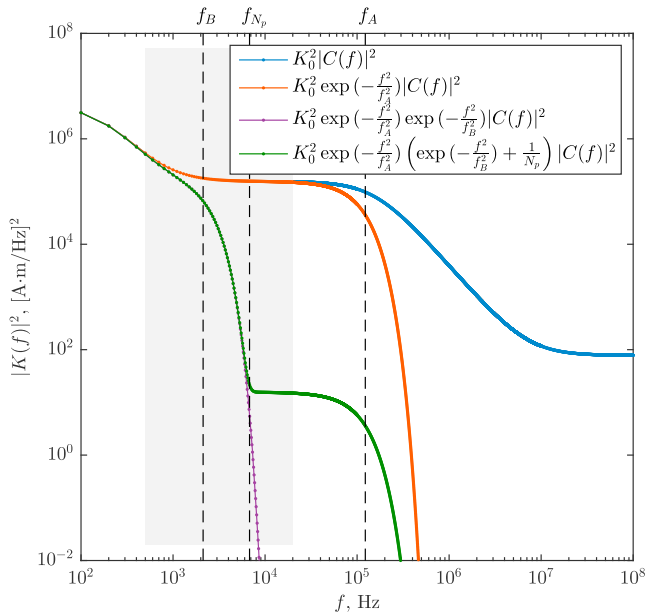
Figure 2. Energy spectrum of the TGF source current moment. Blue line: the spectrum of the total current composition in case if all N_{TGF} runaway electrons ran instantaneously. Red line: if all runaway electrons ran in a single avalanche (modulation of the spectrum by a single RREA and a seeding pulse spectrum). Purple line: modulation by the spectrum of the TGF time profile at source. Green line: all runaway electrons are organized into $N_p = 10^4$ avalanches. Three characteristic frequencies f_A, f_B, and f_{N_p} are shown as black vertical dashed lines. The frequency range of the observed VLF sferics is highlighted by the gray background rectangle (500 Hz to 20 kHz).
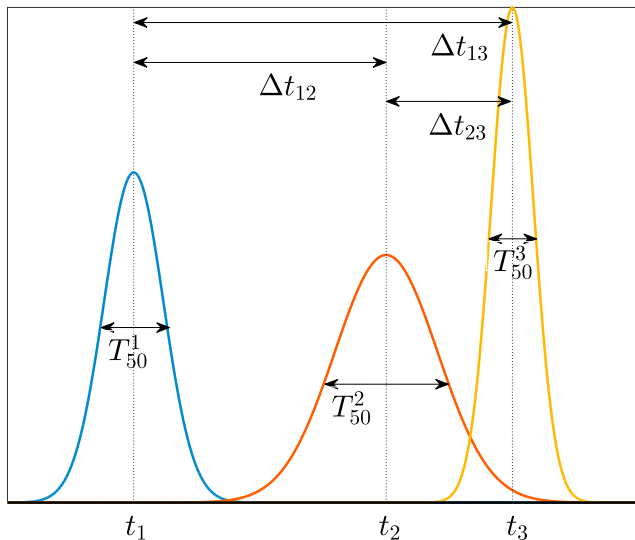

Figure 3. Schematic representation of a complex TGF consisting of three separate peaks. Peak durations T_{50}^k, peak times t_k, and interpeak separation times Δt_{kj} are shown.

peak value t_k: $f_k(t - t_k) = f_k(t_k - t)$. For such a TFG structure the ensemble average gives

$$\frac{1}{N_{seed}^2}\left\langle |\sum_{k=1}^{N} \alpha_k S_k(\omega)|^2 \right\rangle_{\{f_k\}} = \sum_{k=1}^{N} \alpha_k^2 N_{p_k}^2 \left(|f_k(\omega)|^2 \frac{N_{p_k}-1}{N_{p_k}} + \frac{1}{N_{p_k}} \right) + 2\sum_{j<k}\alpha_j\alpha_k N_{p_j} N_{p_k} f_j(\omega)f_k(\omega)\cos(\omega\Delta t_{kj}). \tag{9}$$

Here $S_k(\omega)$ is the spectrum of a seeding flux of the kth TGF peak:

$$S_k(\omega) = N_{seed}\exp\left(-\frac{\omega^2\sigma_s^2}{2}\right)\sum_{j=1}^{N_{p_k}}\exp(i\omega t_j), \tag{10}$$

where t_j is the peak time of the jth seeding pulse within the kth TGF peak.

Consider the simplest case of a TGF consisting of two identical peaks ($\alpha_1 = \alpha_2 = 1$, $N_{p_1} = N_{p_2} = N_p$) separated by a time interval Δt. For such a TGF the expression in square brackets of the source current moment energy spectrum (2) transforms into

$$2\left[\left(\frac{N_p - 1}{N_p} + \cos(2\pi f\Delta t)\right)\exp\left(-\frac{f^2}{f_B^2}\right) + \frac{1}{N_p}\right]. \tag{11}$$

This type of additional modulation by $\cos(2\pi f\Delta t)$ is immediately seen in the energy spectrum when compared with the single-peak TGFs. Notice that this additional modulation only affects the frequencies below f_{N_p}.

The examples of the energy spectra of the source current moments of two modeled double-peak TGFs are given in the Figure 4. These two examples correspond to the TGFs with short-peak durations $T_{50}^1 = T_{50}^2 = 15\,\mu s$ for both TGFs and peak separation times Δt equal to 48 and 135 μs (explanations on T_{50} measuring are given in section 4). The red curve in the Figure 4 corresponds to the event with smaller-peak separation time $\Delta t = 48\,\mu s$. The green curve represents the TGF with longer-peak separation time $\Delta t = 135\,\mu s$. The blue curve shows the energy spectrum of the current moment of a single-peak TGF with the same peak duration $T_{50} = 15\,\mu s$. Such a short-peak duration leads to the cutoff frequency $f_B = 14.1$ kHz, and $f_{N_p} = 45.1$ kHz for the number of seeding pulses $N_p = 10^4$ (see next sections for details). The gray rectangle highlights the frequency range of the VLF recording. In section 5 we show two events with similar characteristics. Here we want to illustrate the fact that the multiplicity of TGF peaks (or any other type of a superstructure) makes a dramatic influence on the TGF radio emission spectrum in VLF range.

2.3. EIWG Transfer Function
The sources of all analyzed VLF sferics were located within a distance range between 2,000 to 4,000 km. Radio waves experience multiple reflections from the ionosphere and ground along their propagation path, which substantially distorts the energy spectrum of the received sferics compared with the source spectrum. The evaluation of the EIWG transfer functions for each event has to account for these propagation effects.

The EIWG transfer function for each individual event was calculated by using the full wave method, described in Lehtinen and Inan (2008, 2009) and Lehtinen et al. (2010). The EIWG transfer function $F_{EIWG}(\omega)$ characterizes how the spectral contents of the radiative source current moment is transferred through the propagation path between the source location and VLF receiver.
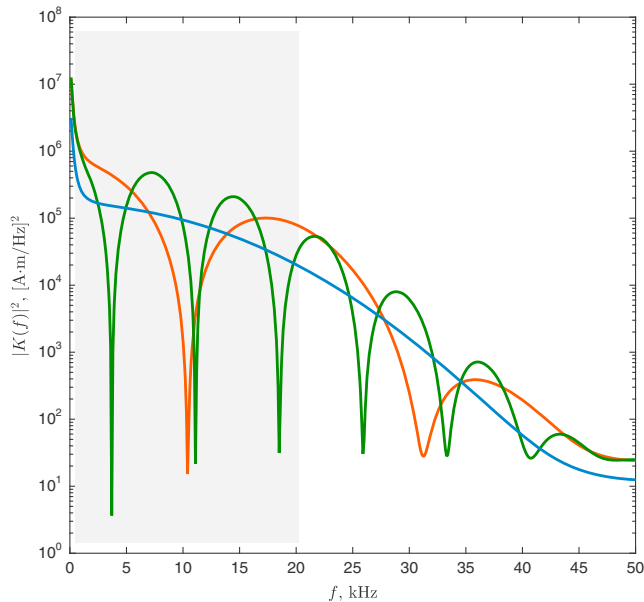
Figure 4. Energy spectra of current moments of two double-peak TGFs with equally short-peak durations T_{50} of 15 μs and peak separation times of 48 μs (red curve) and 135 μs (green curve). Blue curve shows the energy spectrum of the current moment of a single-peak TGF with the same peak duration of 15 μs. Gray rectangle highlights the frequency range of the VLF instrument.

We calculated the propagation of monochromatic electromagnetic waves for the set of frequencies between 0.5 kHz and 16 kHz with the frequency step of 0.5 kHz, and between 16 and 20 kHz with the frequency step of 1 kHz. This frequency range is defined by the VLF sensor and the frequency resolution of 0.5 kHz is due to the 2 ms long time windows used for each VLF sferic, which was optimal in terms of the trade-off between the temporal isolation of the sferics and the frequency resolution of their energy spectra.

The full wave method calculates the propagation of the radio waves in stratified anisotropic media. The source is approximated as a vertical dipole with a current moment of 1 A m located at the TGF source locations at 13 km altitude. The International Reference Ionosphere (Bilitza & Reinisch, 2008) was used to estimate the ionospheric profiles, given the location, season, and local time of each event (IRI is a reasonable guess but is with near certainty not the true D region profile). The International Geomagnetic Reference Field (Thébault et al., 2015) was used to account for the local geomagnetic field along the propagation path.

The current version of the full wave method does not allow to calculate the radio wave propagation with nonvertical geomagnetic field if the curvature of the Earth were to be taken into account. However, it is possible to perform calculations with the Earth curvature and vertical geomagnetic field. We used the following strategy to find the EIWG transfer function, which takes into account both, the realistic geomagnetic field and the curvature of the Earth, thereby extrapolating the result:

1. Calculate the EIWG transfer function with vertical geomagnetic field for the flat Earth.
2. Calculate the EIWG transfer function with vertical geomagnetic field for the curved Earth.
3. Find the transform between these two cases (this transform comprises both the shift of the wave in the direction of propagation and the absolute change in peak amplitudes).
4. Calculate the EIWG transfer function with realistic (nonvertical) geomagnetic field for the flat Earth (most of the analyzed events are located within a compact geographical area, where the geomagnetic field inclination has an approximated value of ≈ 45°. We use this inclination value in the calculation of the EIWG).
5. Apply the transform between the flat and curved cases with vertical field to the last result, which gives the EIWG transfer function with the realistic geomagnetic field with the curvature of the Earth taken into account.

Following the described method, we obtain the EIWG transfer function for the set of frequencies of interest for each event in the analysis.

2.4. Frequency Response of the VLF Sensor

VLF radio recordings were performed by an orthogonal pair of magnetic induction coils that record horizontal magnetic field strengths between 50 Hz and 30 kHz at sampling frequency of 100 kHz. The amplitude frequency response of the VLF coils can be approximated by the following sequence of filters: single-pole high-pass filter at $f_1 = 100$ Hz, single-pole low-pass filter at $f_2 = 12$ kHz, and four-pole low-pass filter at $f_3 = 25$ kHz.

Thus, the frequency response of the VLF instrument can be represented as follows:

$$F_{VLF}(f) = \frac{\left(\frac{f}{f_1}\right)}{\sqrt{1 + \left(\frac{f}{f_1}\right)^2}\sqrt{1 + \left(\frac{f}{f_2}\right)^2}\sqrt{1 + \left(\frac{f}{f_3}\right)^8}}. \quad (12)$$

The frequency response of the VLF instrument $F_{VLF}(f)$ is shown in Figure 5.

2.5. TGF Source Energy Spectrum in VLF Range

Analyzing the structure of the energy spectrum of the TGF source current moment (2), one can see that the spectrum can be naturally split into three distinct frequency ranges: the lower range (below 1 kHz), the middle range (VLF), and the higher range (LF, above ∼100 kHz).
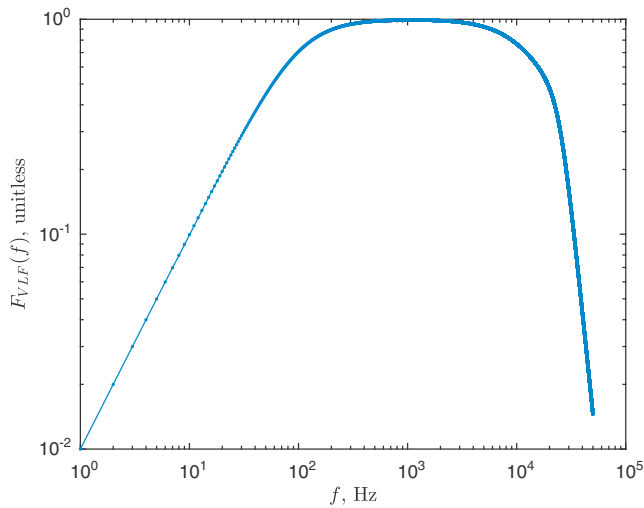
Figure 5. Amplitude frequency response of the VLF instrument $F_{\text{VLF}}(f)$.

The higher range is defined solely by the cutoff frequency f_A. The source energy spectrum in this range simply falls off proportionally to $\exp(-f^2/f_A^2)$. This part of the source spectrum carries the information about the "fast" processes in the TGF source: the seeding pulses and their acceleration and multiplication as RREAs. Note that in the framework of the proposed model, it is impossible to separate a RREA from its seeding pulse (see equation (6)). With the characteristic RREA parameter values accepted in Dwyer and Cummer (2013) for the 13 km source altitude (RREA thickness $\kappa = 220$ m and propagation velocity $v = 0.89c$) RREA duration is of the order of a microsecond ($\kappa/v = 0.82$ μs). This gives the first cutoff frequency $f_A = 123$ kHz (for seeding pulse width $\sigma_s = 1$ μs). Note that shorter seeding pulses (which might be more realistic) and shorter RREAs (which also seem to be more realistic if we were to consider the high E field zone of the negative stepped leader) will give higher values for the cutoff frequency f_A. This means that in real sferics the fast processes in the TGF source do not affect the VLF range, because their spectral term $\exp(-f^2/f_A^2)$ has the constant value close to 1 within the entire VLF range.

The lower range for the frequencies below 1 kHz is dominated by the "slow" ion currents. The more correct way to consider these currents has to exploit the nonlinear approach (ion-ion recombination is a nonlinear process) which does not allow to find an analytical solution in general case. The ion currents may give information about the TGF impact on the air chemistry; however, this complicated problem is out of scope of the current work.

We focus our efforts on the VLF frequency range, the middle range of the TGF source spectrum. The energy spectrum of the source current moment in this range is defined by two independent factors: the second cutoff frequency f_B and the number of seeding pulses N_p (see the term in square brackets in the equation (2)). The cutoff frequency f_B controls the exponential roll-off of the spectrum in VLF range above this frequency as $\exp(-f^2/f_B^2)$. The number of seeding pulses N_p, in turn, sets up a lower limit on the spectral amplitude as $1/N_p$ (the flat shoulder of the green curve in the Figure 2). The larger the value of N_p, the lower the energy spectrum level in the middle range is.

Thereby, f_B defines the spectral roll-off in VLF range, and N_p controls the depth of this roll-off, which can be understood as an internal noise level of the TGF source energy spectrum. In case of real radio recordings, it is important to know how this TGF internal noise level relates to the ambient natural noise level in the VLF range at the receiver's location. For example, if N_p is very high, then the TGF noise level is very low and it might be completely buried in the natural radio noise. In this case the information about the value of N_p will be lost in real VLF sferics. On the other hand, if N_p is relatively small and the TGF noise level is higher than the natural radio noise, then the number of seeding pulses N_p constituting a TGF can be retrieved from its VLF sferic, which is impossible for satellite observations of TGFs. Thus, this circumstance makes VLF recordings an important instrument of TGF observations which may shed some light onto the TGF generation mechanisms.

Another important issue about this $1/N_p$ internal noise level of the TGF source energy spectrum is the frequency f_{N_p} where this flat shoulder actually starts from. We define f_{N_p} as a frequency where the contribution of the exponential term $\exp(-f^2/f_B^2)$ constitutes a $1/e$ part of $1/N_p$: $\exp(-f_{N_p}^2/f_B^2) = 1/eN_p$. This gives

$$f_{N_p} = f_B\sqrt{1 + \log N_p}. \tag{13}$$

Thus, the structure of the source energy spectrum in VLF range consists of two intervals: for frequencies below f_{N_p} the spectrum is driven by the exponential term $\exp(-f^2/f_B^2)$; for frequencies above f_{N_p} the spectrum is proportional to the constant level of $1/N_p$. Note that the boundary frequency f_{N_p} itself is mainly defined by f_B.

In real radio recordings the upper bound of the spectrum is limited by the instrument's frequency range. In our case we are limited by the upper bound of 20 kHz because there is not much energy in the signals above 20 to 25 kHz due to the frequency response and signal attenuation above this frequency. Thereby, in cases when the value of f_{N_p} is higher or comparable with the upper bound of 20 kHz, then the flat shoulder of the source energy spectrum appears to be outside of the frequency range of the VLF instrument. In such a case
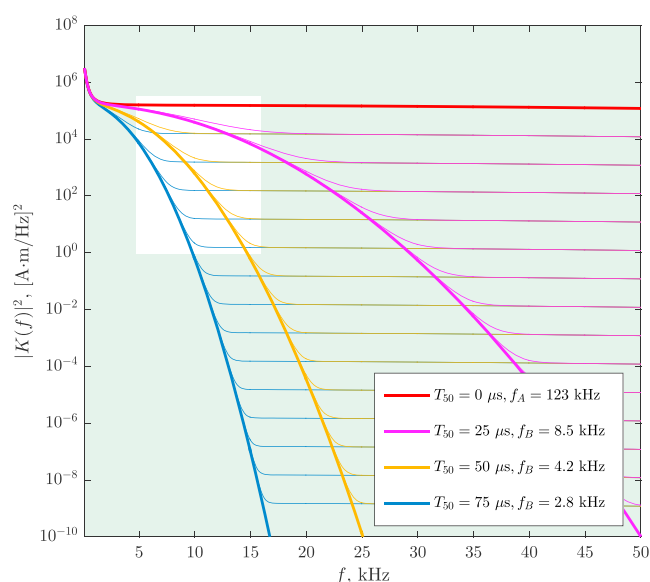
Figure 6. Energy spectrum of the current moment of a single-peak TGF for different values of T_{50} and N_p. N_p varies as 10^k, where k changes from 0 to 14. Each horizontal line corresponds to a certain k value. The upper curve (thick red line) represents a TGF consisted of a single RREA, that is, $N_p = 10^0$. The first cutoff frequency f_A thereby defines the whole spectrum and $f_A = 123$ kHz. The families of magenta, orange, and blue curves show the TGFs with T_{50} equal to 25, 50, and 75 μs correspondingly. Each next horizontal line (going top to bottom) corresponds to the incrementing value of N_p by an order of magnitude. The white rectangle shows schematically the observable diapason of the VLF instrument, bounded by the frequency range between 5 and 15 kHz and by the dynamic range of the instrument (~5 orders of magnitude).

the value of N_p cannot be retrieved from our VLF recordings, though they allow an assessment of the lower limit of N_p.

Another difficulty of practical character concerns the natural VLF noise level. Below 15 kHz it is defined by the global thunderstorm activity, but above that frequency the VLF range is populated by the submarine transmitters. The last circumstance along with the lower-energy deposits in the signals makes the measurements above 15 kHz less reliable. Also, the EIWG transfer function has a significant dip around 3 kHz. Thereby, we focus our analysis on the frequency range between 5 and 15 kHz. This frequency range corresponds to the traditional lightning sferics band, where the returns stroke is typically measured around 10 kHz.

The illustration of the energy spectrum of TGF source current moment for different values of T_{50} and N_p is given in Figure 6. The thick red curve corresponds to the case of a single seeding pulse in a TGF; in this case $N_p = 1$, which eliminates the $\exp\left(-f^2/f_B^2\right)$ term from the spectrum (2). The first cutoff frequency f_A is equal to 123 kHz. Each next horizontal line from top to bottom corresponds to an increase of the N_p value by an order of magnitude: $N_p = 10^k$, where k is the number of the line after the red thick curve. The family of magenta curves shows the spectra of the TGF with $T_{50} = 25$ μs. The orange curves correspond to the TGF with $T_{50} = 50$ μs, and the blue curves relate to the TGF with $T_{50} = 75$ μs. The white rectangle shows the schematics of the observable frequency range in the real VLF recordings that we focus on 5 to 15 kHz frequency range and about 5 orders of magnitude between the signal and the natural noise level (in reality about 4).

From Figure 6 one can conclude that relatively small values of $N_p \leq 10^4$ could be observed and retrieved from the VLF spectra of TGF radio emission for relatively long lasting TGFs with $T_{50} \geq 50$ μs. The shorter TGFs tend to radiate in the higher frequencies which does not allow to retrieve the information about the N_p value (if it is relatively high) from the VLF spectra. Wideband instruments with high dynamic range might help to partially resolve this type of a limitation.

3. Data: Selection Criteria

In this work we investigate simultaneous TGF-VLF pairs. The presented TGFs were detected by RHESSI above the Caribbean region between September 2004 and November 2011. TGFs were identified from RHESSI data (Smith et al., 2002) by use of the off-line search algorithm developed by Gjesteland et al. (2012). RHESSI timing corrections were adopted from Mezentsev et al. (2016). WWLLN detections simultaneous (at the source) within 100 μs uncertainty provided the source locations for the TGF origins. The source altitude for all TGFs was assumed to be equal to 13 km (Cummer et al., 2014, 2015).

VLF magnetic field recordings corresponding the WWLLN sources were recorded by the Duke VLF receiver (Cummer et al., 2005). VLF sensors are deployed at Duke University (35.975°N, 79.094°W) as a pair of magnetic induction coils that record horizontal magnetic field strengths between 50 Hz and 30 kHz, sampled at 100 kHz with the frequency response described in the previous section. Timing accuracy of the VLF sensor is not worse than ∼ 20 μs which allows to attribute confidently recorded sferics to TGFs and WWLLN sources.

The WWLLN database was used to get the geolocations and occurrence times of the analyzed events with the average accuracy of ∼5 km and ∼15 μs (Hutchins et al., 2012; Rodger et al., 2005, 2006).

The main corps of the data for the analysis consists of several tens of TGFs with simultaneous WWLLN detections and associated VLF sferics. The events used in the analysis were selected by the following criteria: sferic criteria, TGF criteria, and source origin criteria.

Sferic criteria include mainly the requirements about the isolation of the sferic from other sferics and the cleanness of its waveform. All unusually looking waveforms were excluded from the analysis as being most likely

the result of an interference with other sferics or with noise (after 2011 the recordings are polluted by the regular pulsed noise presumably coming from the inverter). The isolation criterion was chosen in such a way that the 2 ms time window centered on the sferic waveform could be extracted from the time series without picking up any other waveform, to avoid spectral contamination from other sferics. Also, the signal-to-noise ratio had to be at least of the order of 10^2 at spectral maximum of the sferic.

TGF criteria introduce the limitations on the number of photon counts. As long as we aim to find the link between the TGF and VLF characteristics, we have to be able to calculate reliably the TGF duration in satellite data and relate it to the TGF duration at the source, which requires a relatively high quantity of high-energy photon counts recorded by RHESSI. Thereby, we included in the analysis those TGFs with ≥ 10 photon counts with energies above 100 keV.

Source origin criteria require to consider sources located not further than 4,000 km from Duke VLF receiver, because more distant sources produce sferics with too low signal-to-noise ratio for the analysis. Also, we did not consider very closely located sources, because in this case the sferic waveforms are complicated by many additional features. Thus, we analyzed the sources located between 2,000 and 4,000 km distance from Duke VLF receiver.

4. Fitting Parameters

The energy spectrum (2) of the TGF source current moment is defined by its amplitude K_0, RREA term $\exp\left(-f^2/f_A^2\right)$, seeding flux term (or TGF structure term), and the total current composition term $|C(f)|^2$. In the VLF range the RREA term and the total current composition term stay constant, so for a single-peak TGF its source energy spectrum in VLF range is controlled by only three independent parameters: the total path length of all runaway electrons Ω, the second cutoff frequency f_B, and the number RREAs N_p (which is the same as the number of seeding pulses—each distinct seeding pulse develops into a distinct RREA).

The total path length of all runaway electrons in a TGF Ω (see equations (5), (2), and (3)) defines the amplitude level of the spectrum. We keep Ω as an open parameter which allows us to regulate the amplitude of the modeled spectrum. As a reference value for Ω one can use a value of $2.2 \cdot 10^{20}$ m adopted in Dwyer and Cummer (2013) for a TGF source located at 13 km altitude, which corresponds to the total number of runaway electrons $N_{TGF} = 10^{17}$ (Dwyer & Smith, 2005).

The other two parameters define the shape of the spectrum in VLF range. The cutoff frequency f_B is defined by the TGF time profile width σ_{TGF} at source (see equation (7)), which (with certain precautions) can be related to the measured TGF duration T_{50} at the satellite (assuming the Gaussian distribution for the TGF time profile):

$$\sigma_{TGF} = 0.75 T_{50}. \tag{14}$$

We measure T_{50} of each RHESSI TGF as a time interval between the first 25% and first 75% of the photon counts with energies above 300 keV. Thus, T_{50} makes a link between the satellite observations of TGFs and the ground-based recordings of their radio emissions:

$$f_B = \frac{1}{1.5\pi T_{50}}. \tag{15}$$

The number of RREAs N_p constituting a TGF stays as an open parameter, and we vary its value to provide the best fit between the modeled and observed energy spectra of TGF radio emissions. Values of N_p for each event were varied in a logarithmic scale to estimate how an increase in N_p by 1 order of magnitude changes the energy spectrum shape. We varied N_p values between 10^0 and 10^{14} with a step of one order of magnitude.

For the double-peak TGFs we had to measure the values of T_{50} for both peaks: T_{50}^1 and T_{50}^2, and their separation time Δt. Due to small number of photon counts, these quantities could not be measured with some reliable uncertainty; therefore, we tend to consider these results as questionable, though somehow illustrative, making another link between the satellite and ground-based measurements of TGFs. For simplicity the number of pulses constituting each peak in a double-peak TGF were supposed to be equal: $N_{p_1} = N_{p_2} = N_p$. Thus, for the double-peak TGFs we measure the values of the peak durations T_{50}^1 and T_{50}^2, peak separation time Δt and keep Ω and N_p as open parameters which control the amplitude and shape of the modeled spectra.

Table 1
Occurrence Time, Source Location, Source-to-Duke, and Source-to-Subsatellite-Point Distances

Ev #	Event date	Source time (UTC)	Source location, (latitude, longitude), (°N, °E)	S-Duke (km)	S-sSat (km)
1[a]	11 Sep 2011	08:25:53.548138	(7.6825, −65.4409)	3,427	297
2[a]	11 Sep 2006	04:17:08.476349	(16.1744, −98.0895)	2,891	192
3	11 Sep 2004	07:54:03.499956	(12.1111, −72.2022)	2,733	79
4[b]	31 May 2011	08:17:56.852317	(6.9742, −74.0174)	3,253	306
5	8 Sep 2011	20:31:58.166434	(9.3275, −68.3483)	3,146	297
6[b]	4 Nov 2011	07:54:52.209849	(6.9439, −63.8950)	3,569	209

[a]TGFs treated as double-peak TGFs by their contribution into VLF sferic. [b]Double-peak TGFs with radio emissions simultaneous with the second peak (Mezentsev et al., 2016).

A few words have to be said about how to identify and distinguish double-peak TGFs from single ones. Here we can propose two criteria. The first one applies when the TGF photon flux evidently appears in a form of two distinctive clusters. In this case we just have to measure the durations of the clusters and the time separation between them. Another criterion applies when the photon flux does not show a two-peak structure so evidently, for instance, because of the small amount of photons in the whole TGF. However, if the radio sferic waveform explicitly demonstrates features of being a superposition of two pulses (that can be seen from the shape of the envelope of the sferic waveform), then we have to return to the TGF photon flux and examine it for the possibility of being a combination of two clusters. In this case we have to vary the parameters within the plausible range trying to get the best fit between the modeled and measured spectra. But, for instance, if the best fit between the modeled and measured energy spectra is achieved for a two pulse TGF representation with the peaks separation time which is longer than the total TGF duration, then such a TGF representation is inconsistent with the observed RHESSI data.

5. Results

In this section we report the results on comparing the energy spectra of recorded VLF sferics and modeled radio emissions from TGFs simultaneous with those sferics. From the corps of several tens of events we selected four single-peak TGFs whose modeled VLF energy spectra are consistent with the observed VLF sferics. Also, we report the results on two TGFs with photon fluxes that allow a representation in a form of a double-peak TGF with temporal characteristics producing the modeled VLF energy spectra consistent with the observed VLF sferics whose waveforms and spectra clearly refer to a double-pulse structure.

Table 1 lists the occurrence characteristics of the events: occurrence date and time (UTC, defined by WWLLN), source location (defined by WWLLN), distance between the source and Duke VLF receiver, and distance from the source to the RHESSI subsatellite point. To quickly infer the propagation conditions one might subtract 5 h from the UTC time to get a rough estimate of the local time (LT) of the event and see if that corresponds to the day or the nighttime propagation. The exact values for the source LT and the Duke LT are given below in the detailed description of the events.

Table 1 includes four events which we treat as single-peak TGFs based on their photon flux and VLF sferic energy spectrum, which are characteristic for single-peak events. However, these single-peak events include two evident double-peak TGFs (event numbers 4 and 6, marked by superscript "b" in Table 1). These two double-peak TGFs have been reported in Mezentsev et al. (2016). Both of these events exhibit two clearly distinct peaks separated by 1.7 ms (event number 4) and by 0.5 ms (event number 6). In both cases the radio sferic is simultaneous with the last (second) TGF peak without any noticeable radio emission above the noise level corresponding to the first peaks of these two TGFs. This interesting phenomenon was reported and discussed in detail in Mezentsev et al. (2016). Thereby, considering the TGF and its related radio emission, we treat these two TGFs (more strictly only their second peaks) as single-peak TGFs.

Also, Table 1 contains two events (numbers 1 and 2) which clearly exhibit their double-pulse features in VLF sferics (both in waveforms and in energy spectra). However, the time separation between the two peaks should be small to correspond the observed spectral features: 135 μs and 48 μs correspondingly. Such small values of the peak separation time Δt makes it hard to distinguish the two separate peaks in the photon

Table 2
Fitting Parameters of the 6 TGFs With WWLLN Detections

Ev #	Ω (m)	N_p	T_{50} (μs)	f_B (kHz)	T_{50}^1 (μs)	T_{50}^2 (μs)	Δt (μs)
1	5.5×10^{20}	$\geq 10^3$	(76)	14.15	15	15	48
2	2.8×10^{20}	10^1	(168)	14.15	15	15	135
3	2.8×10^{20}	$\geq 10^3$	35	6.06	–	–	–
4	5.5×10^{20}	10^1	75	2.83	–	–	–
5	4.4×10^{20}	$\geq 10^2$	20	10.61	–	–	–
6	5.5×10^{20}	$\geq 10^1$	12	17.68	–	–	–

flux in RHESSI recordings. However, the recordings for these two events do allow such a representation of these two TGFs in the form of two consecutive pulses with the small separation times of 135 μs and 48 μs correspondingly.

Table 2 gives the overview of the fitting parameters values for the analyzed events. The total path length Ω of all runaway electrons in a TGF corresponds well all the analyzed events with the reference value of $2.2 \cdot 10^{20}$ m adopted from Dwyer and Cummer (2013). This coincidence by itself could serve as a good indicator of a consistency between the TGF radio emission model and real measurements. In case of double-peak events the Ω value refers to a single TGF peak, whereas the total TGF is constructed of two such peaks.

Number of seeding pulses N_p for most of the events shows the lower boundary of possible N_p values, because for the most cases a clear distinction between different N_p values can be made only at higher frequencies due to short durations of the events (i.e., due to high values of the second cutoff frequency f_B; see Figure 6). Only for a relatively long event number 4 the distinction region between different values of N_p lies within the frequency range of interest. For the double TGFs (event numbers 1 and 2) the N_p value was assumed to be the same for both pulses for simplicity.

TGF durations T_{50} listed in Table 2 represent the values that provide the best fit between the modeled and observed VLF energy spectra. For single-peak TGFs those values were taken within the intervals between minimal and maximal values measured from the RHESSI photon flux for photons with energies above 300 keV. Minimal and maximal values were inferred by rounding the measured 25% and 75% of photon flux inward and outward to the closest photons correspondingly. Those minimal and maximal T_{50} values are given below when describing each event in more detail. For the two double-peak TGFs (events 1 and 2) the total duration between the first and the last photons is given (in brackets) to provide the duration reference for the complex of two peaks and a delay Δt between them. The second cutoff frequency f_B is calculated based on T_{50} values by use of equation (15).

Last three columns of Table 2 show the durations T_{50}^1 and T_{50}^2 of the first and second peaks of double-peak TGFs (events 1 and 2), and the time delay Δt between the peaks. Same procedure as for single-peak TGFs was applied to measure the durations of the separate peaks in double-peak TGFs. The time delays Δt were determined as follows. In both cases (events 1 and 2) the photon flux and peak separation time are quite low, as a result, TGF photon sequences might not exhibit the evident two-peak structure and the peaks separation could be ambiguous. However, the additional modulation of the radio sferic energy spectrum due to peaks multiplicity allows an estimation of the separation time Δt by using the spectral dips (see Figure 4). In a simple case of two identical peaks the spectral modulation (11) gives for peak separation Δt:

$$\Delta t = \frac{2k-1}{2f_k},$$ (16)

where f_k is the frequency of the kth spectral dip. The estimated Δt value should be consistent with the observed TGF photon sequence.

To justify the peaks separation in the photon flux, we use grouping pattern where the most energetic photons arrive first and the longer tail of the lower-energy Compton scattered photons arrives after. Using such a pattern it is possible to determine the peaks structure of the TGF, measure the peaks durations T_{50}^1 and T_{50}^2, and determine the peaks separation time Δt as a time difference between the first photons of the two TGF peaks. Thereby, multipeak TGFs may serve as a convincing link between the independent radio recordings and satellite TGF measurements.
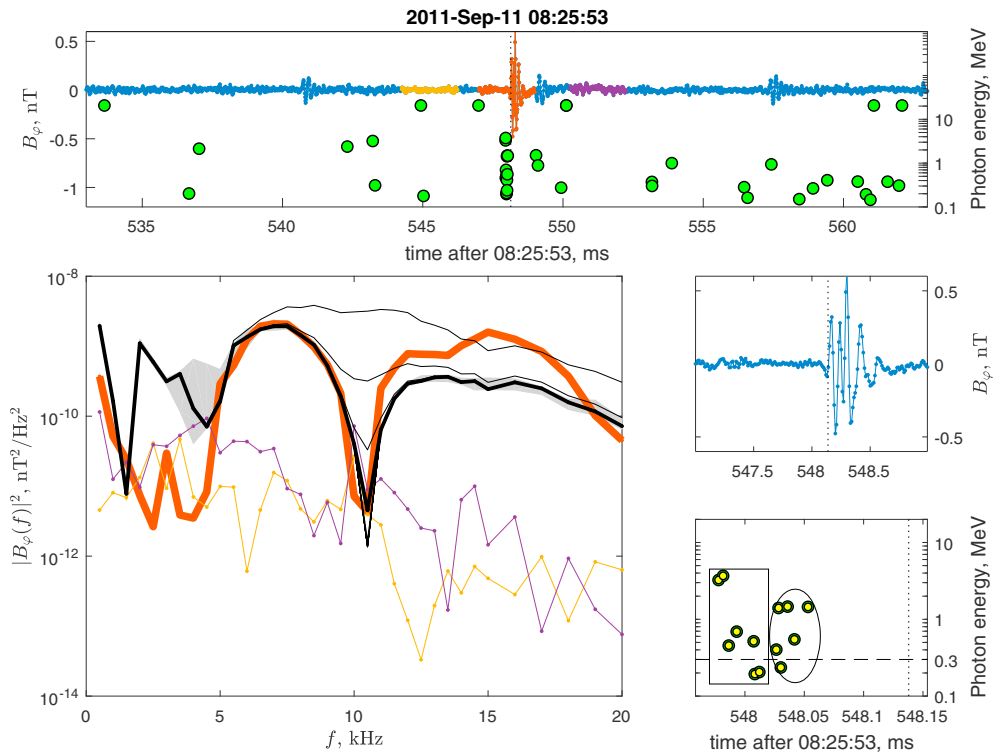
Figure 7. Event 1. Top panel: VLF azimuthal magnetic field (left axis, blue curve; Duke) and photon flux (right axis, green circles; RHESSI) context. Red color highlights the 2 ms sferic waveform taken into analysis. Yellow and purple colors show the 2 ms long pieces of the recording to estimate the noise level before and after the sferic. Big square panel in the left bottom corner shows the energy spectra of the recorded sferic (thick red curve), modeled TGF radio emission with different N_p values (black curves; the best fit is highlighted by the thick black curve), and radio noise before (yellow) and after (purple) the sferic. Two small square panels show the zoomed view on the 2 ms long sferic taken into analysis (top), and the zoomed view on the TGF photon sequence (bottom). See text for more detail.

Below we present the more detailed description of each event. Each description is accompanied by a corresponding figure (Figures 7–12). All these figures are organized in the same manner.

The top panel represents 30 ms of the VLF radio recording of the azimuthal (relative to the Duke-source direction) component of the magnetic field B_φ (left axis), giving the context for a VLF sferic. The radio signal is shown by the blue color, whereas the 2 ms long waveform taken for the analysis, centered on the considered sferic is highlighted by the red color. Another two 2 ms long pieces of the signal, used to estimate the noise level before and after the sferic, are highlighted by the yellow and purple colors, respectively. Green circles show the time versus energy sequence of the RHESSI photons with energies above 100 keV (right axis). Black dotted thin vertical line shows the time of the WWLLN detection. Both, magnetic field and photon flux time axes are recalculated to the WWLLN source location time (expressed as UTC), accounting for the radio wave propagation time to Duke, and for the light travel time to the RHESSI satellite, and for the RHESSI systematic clock offset (Mezentsev et al., 2016).

The large square panel in the bottom left corner of the figures shows the energy spectra. Thick red line represents the energy spectrum of the VLF sferic. The thick black line shows the best fit modeled energy spectrum calculated based on the measured TGF parameters. This modeled spectrum is calculated as it would be observed by the Duke VLF receiver, accounting for the propagation effects in the EIWG and for the frequency response of the instrument (see equation (1)). Gray shaded area around the thick black line indicates the computational error estimate due to the EIWG calculation. This error corresponds the source location accuracy of 50 km. Thin black lines show the modeled spectra for different values of N_p, where they vary logarithmically from 10^0 (the uppermost thin black curve) to 10^{14}, increasing the value of N_p by a factor of 10 on each step (each next thin black curve downward; note that for most of the cases the curves for large values of N_p are indistinguishable from each other in the observed frequency range). Thin yellow and purple curves give the spectra of the noise before and after the studied sferic.
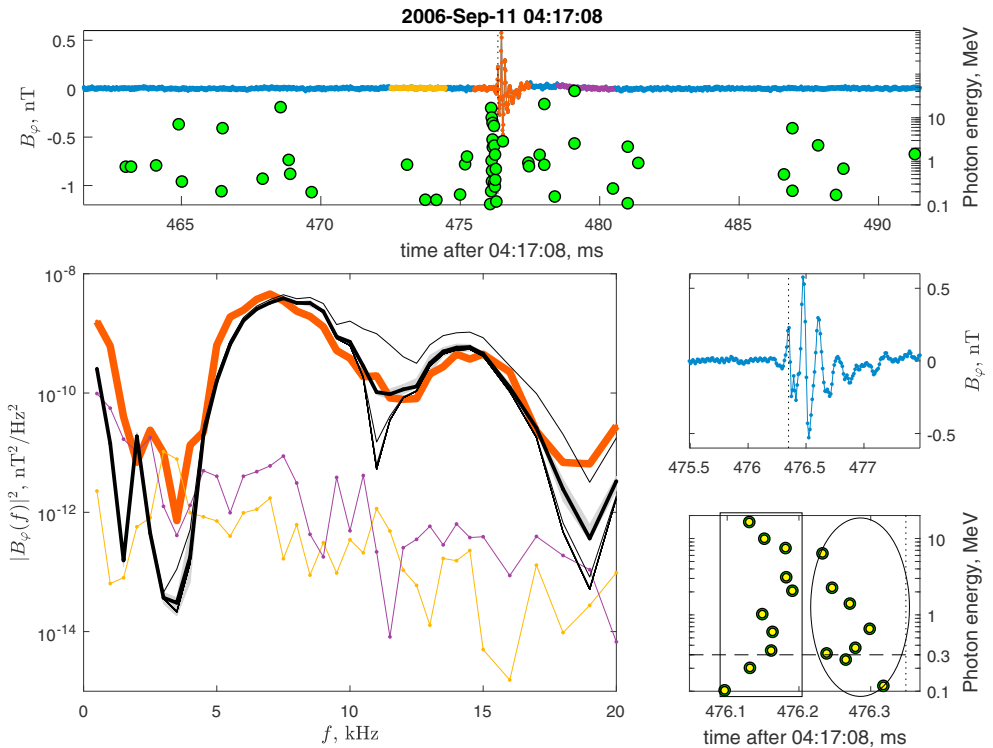
Figure 8. Event 2. Same as Figure 7.

Two small square panels to the right of the spectra block show the zoomed view on the sferic waveform (the top square) and on the TGF photon sequence (the bottom square). Thin dotted black vertical lines show the time of WWLLN detection. Dashed black horizontal line in the TGF photons panel indicates the 300 keV energy boundary. Note that the time axes are not aligned between these two panels and are in slightly different time scales. Also, for the double-peak TGFs (events 1 and 2) the grouping of the photon flux into two distinctive peaks is highlighted by the rectangle and ellipse.

Event 1: 11 September 2011, 08:25:53. Source LT, 04:04:08. Duke LT, 03:09:31. Distance from source to Duke is 3427 km. Source to subsatellite distance is 297 km. VLF sferic is presented by a clear superposition of two strong overlapping pulses (see zoomed sferic panel in Figure 7). The time separation between the two sferic pulses inferred from the energy spectrum is $\sim 48\,\mu s$. Artificial pulses stay aside of the sferic waveform and do not produce interference, but we had to shift the center of the 2 ms time window by 250 μs to the left to avoid picking up one of the artificial pulses.

TGF photon flux consists of 10 photons above 300 keV and allows an interpretation as a sequence of two narrow adjacent pulses (of five photons each—highlighted by a rectangle and an ellipse in the zoomed photon flux panel of Figure 7) with time separation (measured as a time difference between the first photons of the two pulses) $\Delta t = 48\,\mu s$. Two pulses widths T_{50}^1 and T_{50}^2 may vary between 4 and 16 μs for the first pulse, and between 7 and 16 μs for the second pulse. The total TGF duration between the first and the last photons is equal to 76 μs.

Modeled energy spectrum demonstrates the best fit with the observed one for the pulse durations $T_{50}^{1,2} = 15\,\mu s$, pulse separation time $\Delta t = 48\,\mu s$, $\Omega = 5.5 \times 10^{20}$ m, and the lower boundary for the number of avalanches in each pulse of $N_p \geq 10^3$.

Event 2: 11 September 2006, 04:17:08. Source LT, 21:44:47. Duke LT, 23:00:46 (of the previous date). Distance from source to Duke is 2,891 km. Source to subsatellite distance is 192 km. The sferic waveform and its energy spectrum exhibit features characteristic for a superposition of two comparable pulses separated by $\sim 135\,\mu s$ (as determined from the RF energy spectrum).

TGF time profile is presented by a sequence of 14 photons with energies above 300 keV which can be interpreted as a sequence of two distinct comparable pulses of 8 and 6 photons, separated by a delay Δt which
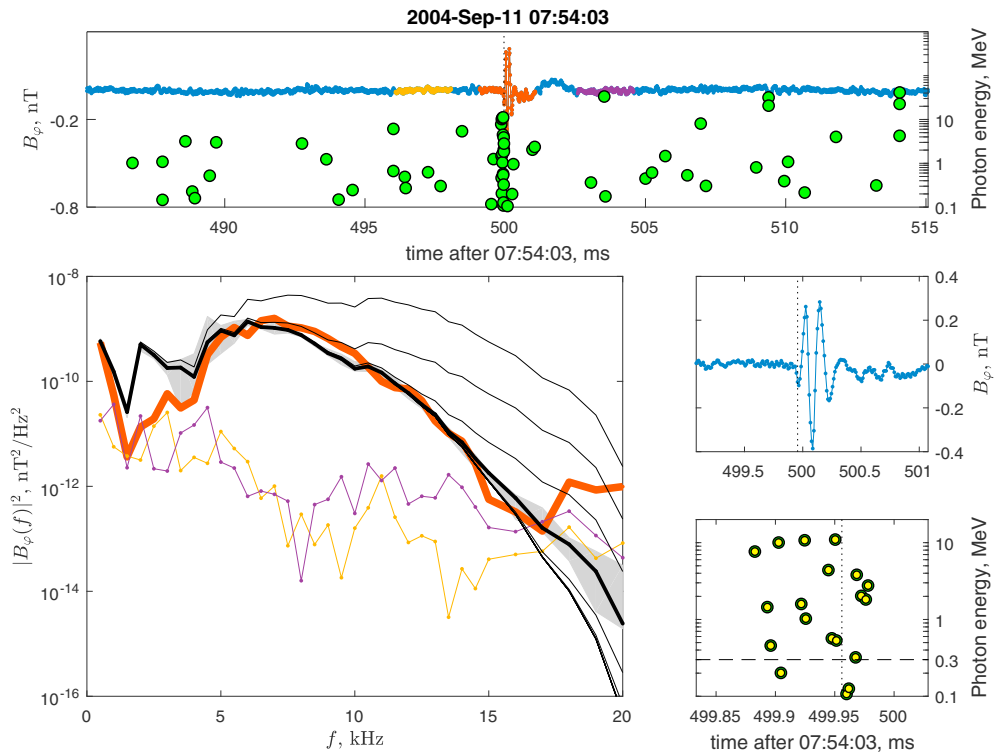
Figure 9. Event 3. Same as Figure 7.

could vary between 103 µs (if Δt is a difference between the first photons above 300 keV of the two pulses) and 137 µs (if Δt is a difference between the first photons of the two pulses including all the photons above 100 keV). The total duration of the TGF between the first and the last photons (above 300 keV) is 168 µs. Pulses widths T_{50}^1 and T_{50}^2 vary between 11 and 52 µs for the first pulse and between 14 and 46 µs for the second pulse. Grouping of the photons into two pulses is highlighted by a rectangle and an ellipse in Figure 8. Modeled energy spectrum fits the observed one best for the pulse durations $T_{50}^1 = 15$ µs and $T_{50}^2 = 15$ µs, pulse separation $\Delta t = 135$ µs, $\Omega = 2.8 \times 10^{20}$ m, and lower boundary for number of seeding pulses $N_p \geq 10$.

Event 3: 11 September 2004, 07:54:03. Source LT, 03:05:15. Duke LT, 02:37:41. Distance from source to Duke is 2,733 km. Source to subsatellite distance is 79 km. The VLF waveform is presented by a clean, single pulse sferic. TGF is presented by 16 photons with energies above 300 keV. The minimal and maximal values for T_{50} define the interval of possible T_{50} values: 29 to 73 µs. The value that gives the best fit between the modeled and observed energy spectra is 35 µs, which refers to the f_B value of 6.06 kHz. The spectral amplitudes fit at the Ω value of 2.8×10^{20} m, which corresponds well the reference value of 2.2×10^{20} m. Relatively high value of f_B does not allow to retrieve the exact value of number of seeding pulses N_p. However, it is possible to estimate the lower boundary for N_p as 10^3 (see Figure 9).

Event 4: 31 May 2011, 08:17:56. Source LT, 03:21:53. Duke LT, 03:01:34. Distance from source to Duke is 3253 km. Source to subsatellite distance is 306 km. All Duke radio recordings from 2011 contain a strong, permanently present artificial feature of a regularly repeated pulsed character ($\sim$ 8 ms separation time between the consecutive pulses, which relates to 120 Hz, the first harmonic of the U.S. power grid). This artifact is most likely related to some inverter, linked to the instrument either through the power chain or through grounding.

VLF sferic is presented by a single pulse, overlapped at its tail by an artificial pulse from the inverter of 2 times lower amplitude. TGF itself is a sequence of two bright distinct TGFs separated by $\sim$ 1.7 ms. VLF sferic and WWLLN detection are simultaneous with the second TGF (see Mezentsev et al., 2016). There is no discernible VLF signal detected in relation to the first TGF. Thereby, we consider the second TGF in relation with the VLF sferic as a single pulse TGF. T_{50} value falls into the interval between 75 and 126 µs. The TGF consists of 11 photons with energies above 300 keV.
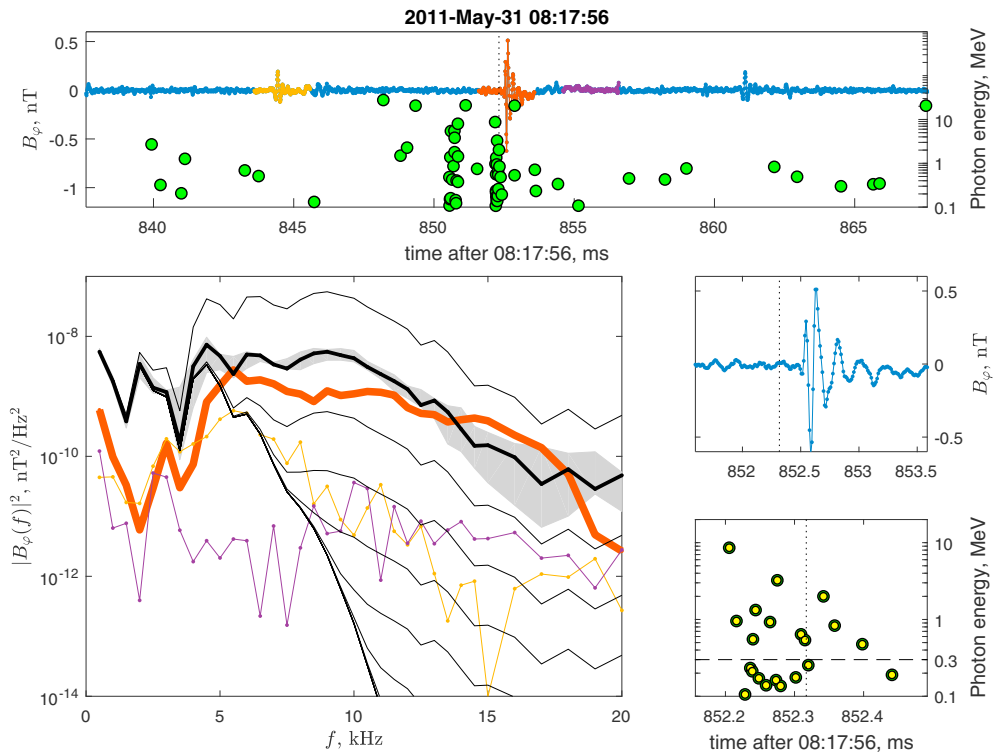
Figure 10. Event 4. Same as Figure 7.

Energy spectrum of the VLF sferic is complicated by the contribution of the artificial pulse from the inverter, whose amplitude is by the factor of 3 lower than the amplitude of the sferic. To estimate the energy spectrum of the artificial pulse itself, we picked up a 2 ms long waveform centered on the artificial pulse (the yellow curves in the top panel of Figure 10). Yellow curve in the spectrum panel of Figure 10 shows that the energy is released by artificial pulses mainly between 3 and 8 kHz (consider the bump at these frequencies that exhibits the yellow curve compared to the purple one, which refers to pure noise). Thereby, it is hard to expect that the observed energy spectrum of the sferic reflects a clear picture of the TGF radio emission. However, the smaller (by the factor of 3) amplitude of the artificial pulse compared to the amplitude of the sferic itself allows an assumption that the spectral distortion by the presence of the artificial pulse is not crucial. Thus, the modeled spectrum with T_{50} value of 75 μs, $\Omega = 5.5 \times 10^{20}$, and $N_p = 10$ provides the best possible fit from the range of possible parameter values.

Event 5: 8 September 2011, 20:31:58. Source LT, 15:58:35. Duke LT, 15:15:36. Distance from source to Duke is 3146 km. Source to subsatellite distance is 297 km. VLF sferic is presented by a single pulse without complications from the artificial pulses. TGF consists of six photons with energies above 300 keV (or 12 photons above 100 keV). T_{50} can vary from 5 to 30 μs. The best fit between the modeled and observed energy spectra is achieved for $T_{50} = 20$ μs, $\Omega = 4.4 \times 10^{20}$ m, and for the lower boundary of $N_p \geq 10^2$ (see Figure 11).

Event 6: 4 November 2011, 07:54:52. Source LT, 03:39:17. Duke LT, 02:38:30. Distance from source to Duke is 3569 km. Source to subsatellite distance is 209 km. We had to shift the center of the 2 ms time window by 300 μs to the left to avoid picking up some other sferic which could distort the spectrum. VLF sferic itself has a waveform which looks like a possible superposition of two overlapping pulses (see zoomed sferic panel in Figure 12) separated by a time delay of $\sim$ 30 μs (due to spectral rise after 15 kHz; see spectral panel of Figure 12). However, the photon flux consists of only seven photons with energies above 300 keV, which does not allow any detailed analysis of the structure of this TGF peak.

We say TGF peak instead of TGF, because this TGF is a double-peak TGF with the weaker first peak (only four photons above 300 keV) and the stronger second peak (seven photons). The peak separation time is $\sim$ 500 μs. WWLLN detection, and VLF sferic are simultaneous with the second TGF peak. No discernible radio emission above the noise level was observed at the occurrence time of the first TGF peak. This event (along with the
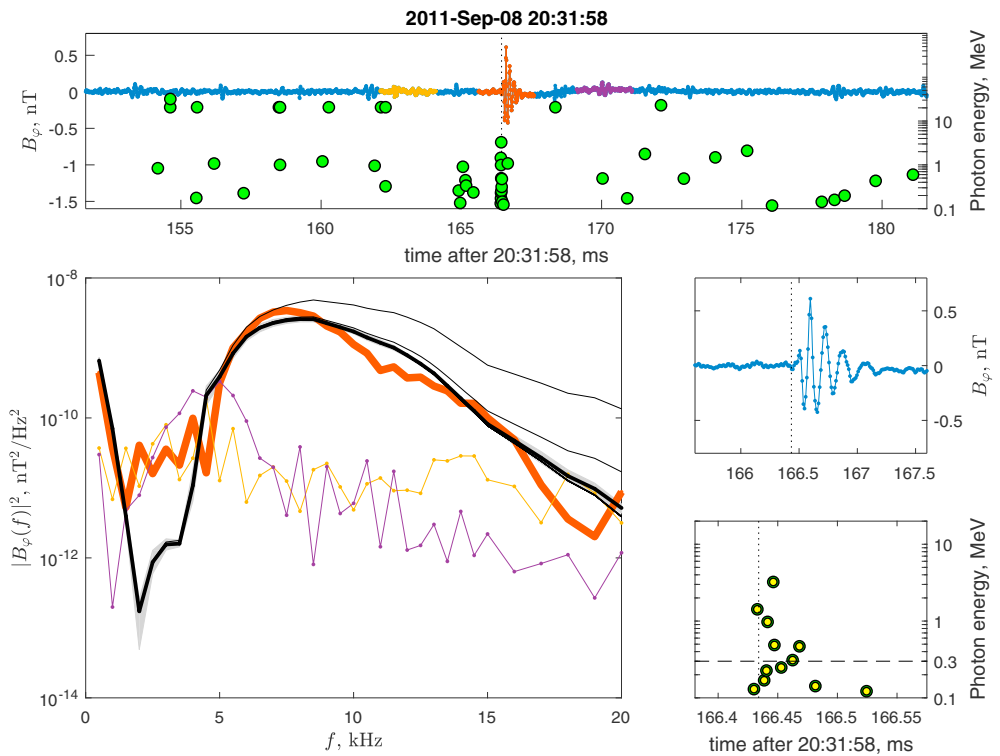
Figure 11. Event 5. Same as Figure 7.

event 3) was also reported and discussed in Mezentsev et al. (2016) in relation with the problem of simultaneity of radio signatures with the last peaks of multipeak TGFs. Here we consider the second TGF peak as a separate single-peak TGF related to the VLF radio signature.

The duration T_{50} may vary between 11 and 23 µs. The best fit between the modeled and the observed energy spectra is achieved for the following parameters values: $T_{50} = 12$ µs, $\Omega = 5.5 \times 10^{20}$ m, and $N_p \geq 10^1$.

6. Discussion and Open Questions

In this section we highlight the difficulties of the practical implementation of the proposed model, its limitations, and discuss the possible scenarios and open questions.

The difficulties are present at every stage of the problem of the TGF radio emission. On the theoretical side there are some open questions with the TGF source structure, with the electric fields used in the model and with the modeling of different processes in the source and their radio emissions. The estimation of the propagation effects in the EIWG is another problem, which cannot be fully solved. On the data side we have problems with reliable estimation of the TGF parameters and its structure due to low photon fluxes and Compton scattering distortions.

A separate problem which stays completely uncovered in our work is the problem of the currents in the lightning leader channel and distinguishing those currents from the TGF source currents, as they may mask each other. Also, we still do not understand the nature of the asymmetry in radio emission of multipeak TGFs (Mezentsev et al., 2016). Below we briefly discuss these questions.

6.1. Difficulties With F_{EIWG} Calculations

In our model the propagation of the EM wave in the EIWG is calculated based on a nonperturbed model of the ionosphere. In case when one or more active thunderstorm cores develop along the propagation path of the radio wave, the ionosphere will be disturbed by the electrical activity of those thunderstorms. These ionospheric disturbances affect the propagation of the EM waves in an unpredictable manner. In the Caribbean region, which was the source location of our data, this is rather common than exceptive situation.
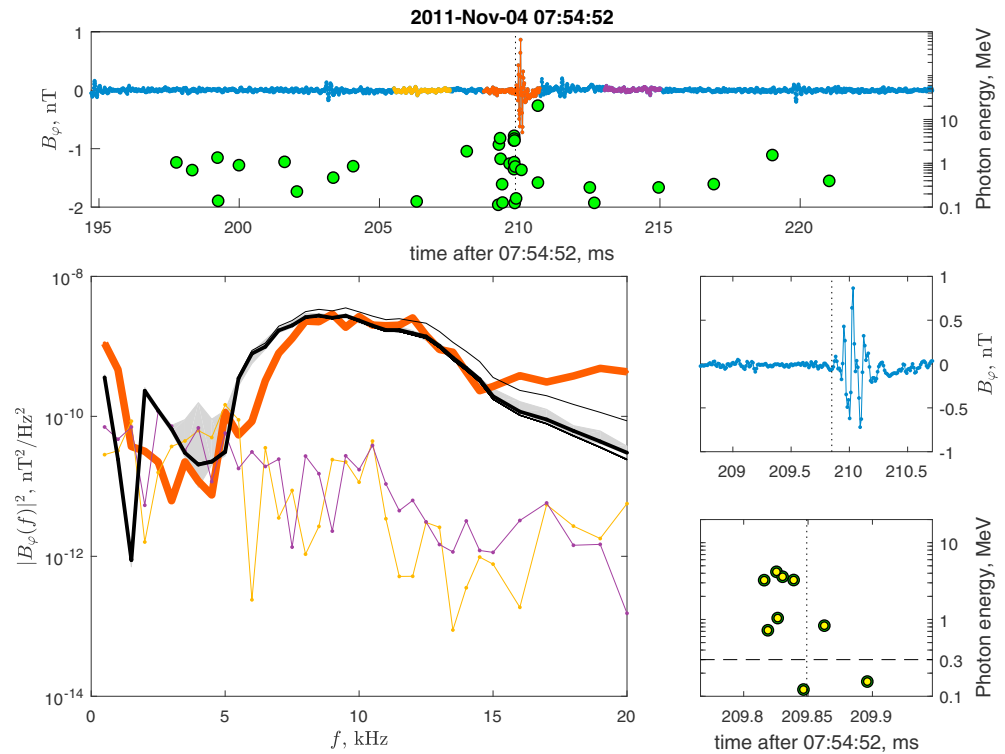
Figure 12. Event 6. Same as Figure 7.

Thus, the main problem with the EIWG transfer function is that one never knows the real ionospheric conditions along the propagation path, which causes deviations of the real EIWG transfer function from the modeled one.

6.2. Different Processes in the Source and Their Frequency Ranges

According to the model of TGF radio emission proposed in Dwyer and Cummer (2013), the energy spectrum of a TGF source current moment exhibits some specific characteristic features which are located in different frequency ranges and reflect different underlying physical processes with their characteristic time scales.

Consider the energy spectrum (2) of the source current moment $|K(f)|^2$. A substantial part of the total energy is emitted in ELF range at frequencies below 1 kHz, (see Figure 2). The emission at these frequencies is defined by the ion currents which have the longest duration due to longest relaxation times ($\tau_{ion} \sim 1$ ms). ELF radio signatures were reported to accompany TGFs usually (see, e.g., Lu et al., 2011), also ELF waveforms can be clearly seen in our results (top panels of Figures 7–12). However, we have to leave the accurate consideration of the ELF part of TGF radio emission for future studies. The ion processes have a nonlinear character which requires a separate study. For the practical purposes of our work it is sufficient to know that the slow ion processes dominate in the frequencies below 1 kHz, though we cannot provide a reliable estimate for those emissions.

In the VLF range the source energy spectrum is totally defined by the TGF source structure. A TGF might consist of several peaks (see Figure 3), each peak is constituted by N_p seeding pulses which follow the time profile $f_{TGF}(t)$ of the peak. This time profile relates to the peak duration T_{50} and defines the second cutoff frequency f_B of the peak (see equation (15)). The cutoff frequency f_B drives the exponential roll-off of the spectrum (as $\exp(-f^2/f_B^2)$) between the frequencies f_B and f_{N_p} (see equation (13) in VLF range. Multiplicity of the TGF peaks modulates the energy spectrum in VLF range (see Figure 4).

Certain precautions have to be made when relating the TGF duration at source and TGF duration at satellite. Dwyer and Cummer (2013) give their arguments that T_{50} measured at the satellite altitude should not differ too much from T_{50} at the source, if only photons above certain energy threshold are included, for example, above 300 keV (same energy threshold with similar arguments was chosen by Gjesteland et al., 2010). Celestin and Pasko (2012) showed that an instantaneous TGF source produces T_{50} of $\approx 50\,\mu s$ at 500 km altitude and

300 km source to subsatellite point distance, due to Compton scattering. However, this T_{50} value refers to the cumulative sum of photons arrived at the satellite, and application of the energy threshold of 300 keV reduces T_{50} to a value of < 10 μs (see Figure 2 in Celestin and Pasko, 2012).

In this sense we would suggest that the TGFs detected by instruments with larger effective area and shorter dead time would give more reliable results in terms of relating T_{50} at the satellite and at the source. Also, TGFs detected when the satellite foot point is closer to the source would be preferable compared to more distant TGFs, because their photons experience less Compton scattering on a shorter path through the atmosphere.

The number of avalanches N_p (which is equivalent to the number of seeding pulses, because each seeding pulse considered here develops into a separate RREA) defines the flat shoulder of the source energy spectrum above the f_{N_p} frequency. This shoulder can be interpreted as an internal noise level of a TGF peak source due to superposition of N_p avalanches.

In the LF range the modulation driven by individual RREAs comes into play. Characteristic durations here are of the order of a microsecond. The source energy spectrum falls off exponentially after the VLF flat shoulder as $\exp(-f^2/f_A^2)$, where f_A has the order of ~ 100 kHz.

6.3. TGF Structure, TGF Duration T_{50}, and Number of Avalanches N_p

The question of the TGF structure is a question of the structure and organization of its seeding flux. A bunch of N_p seeding pulses experiences multiplication via RREA process. In case of a single-peak TGF the total number of runaway electrons N_{TGF} can be represented as a product of three terms: the number of seeding pulses N_p, the multiplication rate N_m, and the number of seeding electrons N_s in an average seeding pulse:

$$N_{TGF} = N_s \cdot N_p \cdot N_m. \tag{17}$$

N_{TGF} is of the order of 10^{17} (Dwyer & Smith, 2005). If the runaway electrons experience a multiplication over ~ 7 avalanche lengths, the multiplication factor N_m is then of the order of $\exp(7) \approx 10^3$. Thus, the overall number of seeding electrons can be estimated as $N_s N_p \approx 10^{14}$. This last assessment shows that larger amount of seeding pulses leads to lower charge carried by the individual seeding pulse.

It is natural to assume that a seeding pulse is localized at least in time (i.e., it is brief), and perhaps in space (i.e., its electrons come out of a small spatial volume all together). As natural candidates producing these seeding energetic electrons organized into seeding pulses one can consider the streamer heads of the streamers in the negative corona flash during the +IC stepping. Number of negative streamers in the negative corona flash can be related then to the number of seeding pulses N_p in a single TGF peak. Several consecutive leader steps with their negative corona flashes could produce a multipeak TGF with several distinct or overlapping brief peaks.

Events 2 and 4 in our analysis (Figures 8 and 10) show that the number of avalanches N_p is rather small, of the order of 10^1. This might imply another type of a TGF structure. Namely, if we are talking about a very small number of avalanches, this lets us coordinate the pulsed nature of a TGF, stretched over a time duration of about a hundred microseconds, with the stepped nature of a negative stepped leader, which exhibits a very similar dynamics. This picture would be consistent with the TGF model discussed in Celestin et al. (2015), where the seeding electrons are launched all in one go during the negative corona flash after the stepping of a negative leader. Within this scenario several consecutive leader steps might generate several consecutive seeding pulses which evolve into RREAs in the electric field of the leader tip (Skeltved et al., 2017).

As an illustration to the last scenario we can refer to our event 3. In the zoomed photon flux panel of Figure 9 one can see four photons with energies of the order of 10 MeV, following each other every ~ 25 microseconds. Such a sequence is unlikely to be the result of a Compton scattering of an instantaneous source (Celestin & Pasko, 2012). It rather looks like a sequence of four independent pulses which could refer to four consecutive negative leader steps. However, we have to notice that for this particular event the lower boundary for N_p is at least of the order of 100, and also a direct simulation of the source current moment in a form of four consecutive pulses does not give a good fit between the modeled and observed VLF energy spectra.

Thereby, it is unclear what kind of process defines the number of seeding pulses N_p in a TGF source. In case when N_p relates to the number of individual streamers in the negative corona flash after stepping, the value of N_p can be large ($\geq 10^4$). However, we do not have the estimate for the number of streamers in the negative

corona flash during the +IC leader stepping. In this scenario several consecutive leader steps can produce a multipeak TGF. In case when N_p relates to the number of several consecutive (short) leader steps, its value should be small, of the order of 10. In our work we proposed the way of how these scenarios can be distinguished by the analysis of the VLF energy spectra of the radio sferics associated with TGFs.

Another possible mechanism for the seeding pulses production could be the large number of backscattered X-rays or backward accelerated positrons, which create the seeding runaway electrons in the production region (Dwyer, 2012). This mechanism should involve a very large number of seeding pulses N_p, of the order of $\sim 10^{14}$, due to equation (17) and $N_s = 1$ (if the feedback factor is close to 1) in this mechanism. However, the data presented in Dwyer and Cummer (2013) report about relatively small number of seeding pulses, $N_p = 10^4$, which corresponds to the "slow lightning source 2" (as it is called in Dwyer & Cummer, 2013). The huge number of seeding pulses N_p required by the feedback mechanism looks to be inconsistent with the observed spectra which show much smaller numbers (10^4 against required 10^{14}).

There is also another difficulty of practical character which makes it impossible to observe very large values of N_p if they would really exist. Namely, it is the level of the natural EM noise, which is at least 10 orders of magnitude higher than the internal RF noise level of a TGF, if it were generated by $N_p = 10^{14}$ seeding pulses, as required by the feedback mechanism.

The analysis performed in the presented work, in turn, shows that the number of seeding pulses N_p is rather small. We can confidently rule out the feedback mechanism for at least two of the presented events. However, the rest of the data only allows us to estimate the lower boundary of the possible value of N_p, thereby, theoretically, we cannot rule out the feedback mechanism from the list of possible scenarios for those events.

Our results show that better understanding of the negative corona flash after the +IC leader stepping, its spatial structure and dynamics is very important for revealing the production mechanism and structure of the TGF source.

6.4. Leader Currents

In this work we only consider the currents directly related to the runaway electrons and their secondaries, assuming these to be the source of the detected radio signals. However, the leader processes and associated currents, which might play a significant role or even dominate in the observed radio emission, are out of scope of the study and thereby have been ignored. This important question stays open.

It is important to point out that detailed observations of at least some TGFs show that there is very high noise present due to other lightning processes happening within the same time window as the TGF (maybe separated by tens to hundreds of microseconds). Cummer et al. (2015) show some examples in which they have the advantage of short propagation distances and higher bandwidth sensors.

Some efforts on featuring and distinguishing the TGF produced radio signatures from lightning related sferics were performed in Lyu et al. (2015) and in Lyu et al. (2016).

Another open question which was first addressed in Mezentsev et al. (2016) and probably also relates to the lightning leader currents is about the asymmetry of the radio emission of multiple peak TGFs. Mezentsev et al. (2016) reported that radio emission for such TGFs is simultaneous with the last TGF peaks. TGF radio emission model of Dwyer and Cummer (2013) does not address such an asymmetry. This might reflect more complex relationships between TGFs and processes in the lightning leaders, which need further clarification.

7. Conclusion

In the presented work we analyze the structure of a TGF source current moment energy spectrum, as proposed in the model of Dwyer and Cummer (2013). We inferred the link between TGF duration and the VLF cutoff frequency f_B in the energy spectrum of TGF radio emission. We test our analysis on six TGFs with known source locations (provided by WWLLN detections) and their simultaneous VLF sferics recorded by Duke VLF receiver. The propagation effects in the EIWG were taken into account by evaluating the EIWG transfer function for each event. The comparisons of the modeled and observed VLF energy spectra were made under the assumption that the TGF source processes (runaway electrons and their secondaries) were responsible for the observed radio signal, or played a dominant role in it, without considering other possible sources of RF emissions from the leader processes.

Two of six events exhibit features of two overlapping pulses, which leads to the analysis of the additional spectral modulation by the multiplicity of TGF peaks with known characteristics (durations and mutual time delays).

Some evidence was found that the number of avalanches in the TGFs is rather small. This might refer to the scenario when a TGF is generated as a sequence of brief gamma ray bursts generated during negative corona flash stages of several consecutive leader steps of the negative +IC leader.

References

Bilitza, D., & Reinisch, B. W. (2008). International Reference Ionosphere 2007: Improvements and new parameters. *Advances in Space Research*, *42*(4), 599–609. https://doi.org/10.1016/j.asr.2007.07.048

Celestin, S., & Pasko, V. P. (2012). Compton scattering effects on the duration of terrestrial gamma-ray flashes. *Geophysical Research Letters*, *39*, L02802. https://doi.org/10.1029/2011GL050342

Celestin, S., & Pasko, V. P. (2011). Energy and fluxes of thermal runaway electrons produced by exponential growth of streamers during the stepping of lightning leaders and in transient luminous events. *Journal of Geophysical Research*, *116*, A03315. https://doi.org/10.1029/2010JA016260

Celestin, S., Xu, W., & Pasko, V. P. (2012). Terrestrial gamma ray flashes with energies up to 100 MeV produced by nonequilibrium acceleration of electrons in lightning. *Journal of Geophysical Research*, *117*, A05315. https://doi.org/10.1029/2012JA017535

Celestin, S., Xu, W., & Pasko, V. P. (2015). Variability in fluence and spectrum of high-energy photon bursts produced by lightning leaders. *Journal of Geophysical Research: Space Physics*, *120*, 10712–10723. https://doi.org/10.1002/2015JA021410

Connaughton, V., Briggs, M. S., Holzworth, R. H., Hutchins, M. L., Fishman, G. J., Wilson-Hodge, C. A., … Smith, D. M. (2010). Associations between Fermi Gamma-ray Burst Monitor terrestrial gamma ray flashes and sferics from the World Wide Lightning Location Network. *Journal of Geophysical Research*, *115*, A12307. https://doi.org/10.1029/2010JA015681

Connaughton, V., Briggs, M. S., Xiong, S., Dwyer, J. R., Hutchins, M. L., Eric Grove, J., … Wilson-Hodge, C. (2013). Radio signals from electron beams in terrestrial gamma ray flashes. *Journal of Geophysical Research: Space Physics*, *118*, 2313–2320. https://doi.org/10.1002/2012JA018288

Cummer, S. A., Zhai, Y., Hu, W., Smith, D. M., Lopez, L. I., & Stanley, M. A. (2005). Measurements and implications of the relationship between lightning and terrestrial gamma ray flashes. *Geophysical Research Letters*, *32*, L08811. https://doi.org/10.1029/2005GL022778

Cummer, S. A., Lu, G., Briggs, M. S., Connaughton, V., Xiong, S., Fishman, G. J., & Dwyer, J. R. (2011). The lightning-TGF relationship on microsecond timescales. *Geophysical Research Letters*, *38*, L14810. https://doi.org/10.1029/2011GL048099

Cummer, S. A., Briggs, M. S., Dwyer, J. R., Xiong, S., Connaughton, V., Fishman, G. J., … Solanki, R. (2014). The source altitude, electric current, and intrinsic brightness of terrestrial gamma ray flashes. *Geophysical Research Letters*, *41*, 8586–8593. https://doi.org/10.1002/2014GL062196

Cummer, S. A., Lyu, F., Briggs, M. S., Fitzpatrick, G., Roberts, O. J., & Dwyer, J. R. (2015). Lightning leader altitude progression in terrestrial gamma ray flashes. *Geophysical Research Letters*, *42*, 7792–7798. https://doi.org/10.1002/2015GL065228

Dwyer, J. R. (2012). The relativistic feedback discharge model of terrestrial gamma ray flashes. *Journal of Geophysical Research*, *117*, A02308. https://doi.org/10.1029/2011JA017160

Dwyer, J. R., & Smith, D. M. (2005). A comparison between Monte Carlo simulations of runaway breakdown and terrestrial gamma-ray flash observations. *Geophysical Research Letters*, *32*, L22804. https://doi.org/10.1002/2005GL023848

Dwyer, J. R., & Cummer, S. A. (2013). Radio emissions from terrestrial gamma ray flashes. *Journal of Geophysical Research: Space Physics*, *118*, 3769–3790. https://doi.org/10.1002/jgra.50188

Fishman, G. J., Bhat, P. N., Mallozzi, R., Horack, J. M., Koshut, T., Kouveliotou, C., … Christian, H. J. (1994). Discovery of intense gamma-ray flashes of atmospheric origin. *Science*, *264*, 1313–1316. https://doi.org/10.1126/science.264.5163.1313

Gjesteland, T., Østgaard, N., Connell, P. H., Stadsnes, J., & Fishman, G. J. (2010). Effects of dead time losses on terrestrial gamma ray flash measurements with the Burst and Transient Source Experiment. *Journal of Geophysical Research*, *115*, A00E21. https://doi.org/10.1029/2009JA014578

Gjesteland, T., Østgaard, N., Collier, A. B., Carlson, B. E., Eyles, C., & Smith, D. M. (2012). A new method reveals more TGFs in the RHESSI data. *Geophysical Research Letters*, *39*, L05102. https://doi.org/10.1029/2012GL050899

Hutchins, M. L., Holzworth, R. H., Brundell, J. B., & Rodger, C. J. (2012). Relative detection efficiency of the World Wide Lightning Location Network. *Radio Science*, *47*, RS6005. https://doi.org/10.1029/2012RS005049

Lehtinen, N. G., & Inan, U. S. (2008). Radiation of ELF/VLF waves by harmonically varying currents into a stratified ionosphere with application to radiation by a modulated electrojet. *Journal of Geophysical Research*, *113*, A06301. https://doi.org/10.1029/2007JA012911

Lehtinen, N. G., & Inan, U. S. (2009). Full-wave modeling of transionospheric propagation of VLF waves. *Geophysical Research Letters*, *36*, L03104. https://doi.org/10.1029/2008GL036535

Lehtinen, N. G., Marshall, R. A., & Inan, U. S. (2010). Full-wave modeling of "early" VLF perturbations caused by lightning electromagnetic pulses. *Journal of Geophysical Research*, *115*, A00E40. https://doi.org/10.1029/2009JA014776

Lu, G., Blakeslee, R. J., Li, J., Smith, D. M., Shao, X.-M., & McCaul, E. W. (2010). Lightning mapping observation of a terrestrial gamma-ray flash. *Geophysical Research Letters*, *37*, L11806. https://doi.org/10.1029/2010GL043494

Lu, G., Cummer, S. A., Li, J., Han, F., Smith, D. M., & Grefenstette, B. W. (2011). Characteristics of broadband lightning emissions associated with terrestrial gamma ray flashes. *Journal of Geophysical Research*, *116*, A03316. https://doi.org/10.1029/2010JA016141

Lyu, F., Cummer, S. A., & McTague, L. (2015). Insights into high peak current in-cloud lightning events during thunderstorms. *Geophysical Research Letters*, *42*, 6836–6843. https://doi.org/10.1002/2015GL065047

Lyu, F., Cummer, S. A., Briggs, M., Marisaldi, M., Blakeslee, R. J., Bruning, E., … Stanbro, M. (2016). Ground detection of terrestrial gamma ray flashes from distant radio signals. *Geophysical Research Letters*, *43*, 8728–8734. https://doi.org/10.1002/2016GL070154

Mezentsev, A., Østgaard, N., Gjesteland, T., Albrechtsen, K., Lehtinen, N., Marisaldi, M., … Cummer, S. (2016). Radio emissions from double RHESSI TGFs. *Journal of Geophysical Research: Atmospheres*, *121*, 8006–8022. https://doi.org/10.1002/2016JD025111

Rodger, C. J., Brundell, J. B., & Dowden, R. L. (2005). Location accuracy of VLF World-Wide Lightning Location (WWLL) network: Post-algorithm upgrade. *Annales Geophysicae*, *23*, 277–290.

Rodger, C. J., Werner, S., Brundell, J. B., Lay, E. H., Thomson, N. R., Holzworth, R. H., & Dowden, R. L. (2006). Detection efficiency of the VLF World-Wide Lightning Location Network (WWLLN): Initial case study. *Annales Geophysicae*, *24*, 3197–3214.

Shao, X.-M., Hamlin, T., & Smith, D. M. (2010). A closer examination of terrestrial gamma-ray flash-related lightning processes. *Journal of Geophysical Research*, *115*, A00E30. https://doi.org/10.1029/2009JA014835

Skeltved, A. B., Østgaard, N., Mezentsev, A., Lehtinen, N., & Carlson, B. (2017). Constraints to do realistic modeling of the electric field ahead of the tip of a lightning leader. *Journal of Geophysical Research: Atmospheres*, *122*, 8120–8134. https://doi.org/10.1002/2016JD026206

Smith, D. M., Lin, R. P., Turin, P., Curtis, D. W., Primbsch, J. H., … Schwartz, R. (2002). The RHESSI spectrometer. *Solar Physics*, *210*, 33–60.

Stanley, M. A., Shao, X.-M., Smith, D. M., Lopez, L. I., Pongratz, M. B., Harlin, J. D., … Regan, A. (2006). A link between terrestrial gamma-ray flashes and intracloud lightning discharges. *Geophysical Research Letters*, *33*, L06803. https://doi.org/10.1029/2005GL025537

Thébault, E., Finlay, C. C., Beggan, C. D., Alken, P., Aubert, J., Barrois, O., … Zvereva, T. (2015). International geomagnetic reference field: The 12th generation. *Earth, Planets and Space*, *67*(1), 1–9. https://doi.org/10.1186/s40623-015-0228-9

Xu, W., Celestin, S., & Pasko, V. (2014). Modeling of X-ray emissions produced by stepping lightning leaders. *Geophysical Research Letters*, *41*, 7406–7412. https://doi.org/10.1002/2014GL061163

Xu, W., Celestin, S., & Pasko, V. (2012). Source altitudes of terrestrial gamma-ray flashes produced by lightning leaders. *Geophysical Research Letters*, *39*, L08801. https://doi.org/10.1029/2012GL051351